

DIII-D Research Advancing the Scientific Basis for Burning Plasmas and Fusion Energy

W.M. Solomon 1) for the DIII-D team

1) General Atomics, San Diego, California 92121, USA

e-mail contact of main author: solomon@fusion.gat.com

Abstract. The DIII-D tokamak has addressed key issues to advance the physics basis for ITER and future steady-state fusion devices. The ITER baseline scenario is challenged at low rotation, where magnetic probing identifies a decrease in ideal stability correlated with changes in the current profile and increased tearing instability, providing a basis for active instability sensing. Improved understanding of 3D interactions is emerging, with RMP-ELM suppression correlated with exciting an edge current driven mode, while core tearing mode drives are mediated through a global kink response. $n = 2$ error fields are found to drive locked mode instabilities at levels similar to $n = 1$. Should plasma termination be necessary, shattered neon pellet injection has been shown to be tunable to adjust radiation and current quench rate; the technique also proves effective in dissipating runaway electron beams. Reduced transport models such as TGLF reproduce the reduction in confinement associated with additional electron heating in ITER baseline plasmas. Raising the pedestal density can recover the performance in the ITER baseline through an increase in the pedestal pressure, and can even give access to Super H-mode for ITER. A new wide-pedestal variant of QH-mode has been discovered where increased edge transport is found to allow higher pedestal pressure, consistent with peeling-ballooning theory. New dimensionless scaling experiments suggest an intrinsic torque comparable to the beam-driven torque on ITER. Complete ELM suppression has been achieved in steady-state “hybrid” plasmas that is relatively insensitive to q_{95} , having a weak effect on the pedestal. Both high- q_{\min} and hybrid steady-state plasmas have avoided fast ion instabilities and achieved increased performance by control of the fast ion pressure gradient and magnetic shear, and use of external control tools such as ECH. In the boundary, $E \times B$ drifts are required in simulations to match observed asymmetries in divertor detachment, and the erosion rate of high- Z materials is found to be reduced through control of the electric field in the pre-sheath. Between-ELM heat flux asymmetries in the presence of RMP fields are determined to be eliminated in detached divertor conditions.

1. Introduction

Research on DIII-D has made significant advances for fusion energy, with a focus on resolving issues critical to the success of ITER, while developing the operational knowledge and scientific basis relevant for next-step fusion devices. Progress has been made in the areas of transient control, transport physics, understanding of core-edge coupling and boundary processes, and integrated steady-state scenarios. Results described in this paper have been obtained by utilizing key developments in the facility (e.g. disruption mitigators, new diagnostics, very high harmonic fast wave [“helicon”] launch), as well as exploiting existing flexibility (e.g. shape control, independent variation of torque and power, decoupled ion and electron heating schemes, adjustable current drive deposition, variable applied 3D field spectra), and dedicated experimental campaigns with tungsten metal tile inserts and helium main ion and beam injection.

The paper is organized as follows. In Section 2, recent advances in the control of transient events, including both ELM control and mitigation of major disruptions is described, plus the first demonstration of runaway electron plateau dissipation using the shattered pellet technique. Section 3 describes research aimed at preparing for burning plasmas, including advances in the physics basis needed to achieve $Q = 10$ performance on ITER and improved understanding of the relevant transport processes. In Section 4, advances in the physics of detachment, detailing the important role of drifts, are presented, together with new insights into the interplay between the divertor and upstream pedestal profiles. Finally, in Section 5, work focused on achieving steady-state performance for both ITER and future fusion reactors is discussed, with an emphasis on the integration of both the appropriate boundary solutions (ELM control and radiative divertor) and techniques for mitigating anomalous thermal and fast ion transport.

2. Control of Transient Events

A Achieving high performance with robust ELM control

High confinement operation in H-mode is generally associated with strong gradients in the profiles near the edge, or so-called “pedestal” region. These strong gradients are observed to trigger edge localized modes (ELMs) [1], which result in repetitive bursts of energy and particles being expelled from the pedestal, and are a serious concern to the integrity of plasma facing components. DIII-D is pursuing several parallel lines of research to address this challenge, through the suppression of ELMs with resonant magnetic perturbations (RMP) [2], pellet pacing [3, 4], and naturally ELM-stable regimes such as Quiescent H-mode (QH-mode) [5].

New insights into the physics of RMP ELM suppression in ITER baseline conditions have been obtained providing more confidence in projecting to ITER. Measurements have revealed that ELM control requires the applied field to couple to a stable MHD mode near an edge rational surface, with such a response directly observed on high field side (HFS) magnetic sensors at low q_{95} on DIII-D, typical of ITER baseline conditions. The measured edge HFS response is found to be inversely proportional to the pedestal collisionality but with no dependence on β_N (Fig. 1), as would be expected for a current-driven mode. This is in contrast to the pressure-driven kink that depends on β_N and is observed on the low field side (LFS). These results elucidate the importance of low collisionality for achieving ELM suppression [6] and supported the first achievement of ELM suppression at ASDEX Upgrade [7].

An emerging scientific picture to describe ELM suppression by RMP fields is that the expansion of the pedestal radially inward is halted by penetration of the field when the electron perpendicular drift velocity is low. This has been supported by measurements in L-mode plasmas showing island formation at the $q = 2$ surface due to an applied field is easiest when the perpendicular electron velocity is near zero [8]. At the onset of ELM suppression, the plasma rotation and density fluctuation levels change rapidly, as well as the amplitude and phase to the HFS magnetics measurements. These changes are indicative of a bifurcation in the transport resulting from penetration of the fields. New experiments have found that ELM

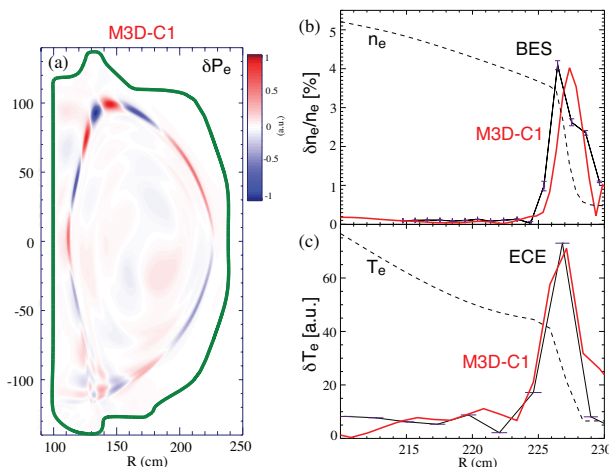


FIG. 2. Fluctuations in (a) pressure, (b) density, and (c) temperature from M3D-C1 and comparison with experimental measurements.

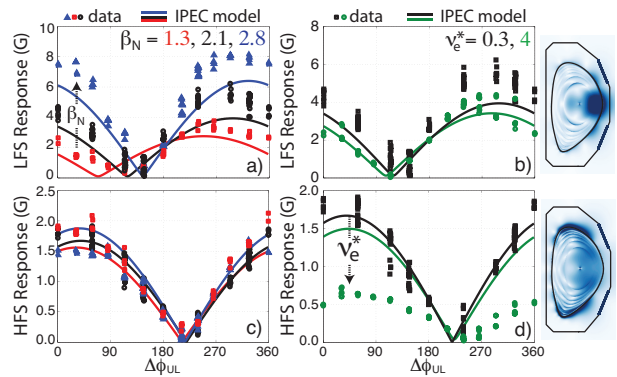


FIG. 1. LFS (top) and HFS (bottom) response as $n = 2$ applied field varied at different β_N and collisionality.

suppression in ITER baseline conditions is lost at reduced toroidal rotation. This is consistent with the need of low electron perpendicular drift velocity to allow field penetration, because co-current rotation is required to counteract the diamagnetic contribution to the flow. Hence, the achievement of ELM suppression in low rotation plasmas at low q_{95} likely requires the optimization of the edge intrinsic rotation drive, non-axisymmetric field-driven torques and the pedestal gradients [6].

As an alternative to actively suppressing ELMs, ITER will also be equipped to pace ELMs with D_2 pellets, aiming to increase the frequency of ELMs with a concomitant reduction in the peak heat flux. DIII-D has extended earlier studies of high frequency ELM pacing with D_2 pellets (≈ 90 Hz or 8 times

the natural ELM frequency) to low rotation conditions anticipated for ITER. High frequency pacing has also been demonstrated with non-fuel Li pellets up to 200 Hz, resulting in a 10-fold increase in ELM frequency, at least transiently [9], as well as shown compatibility with core fueling. For Li pacing, most triggered ELM events show reductions in the heat flux, but a small fraction ($< 10\%$) show heat fluxes comparable to the natural un-paced ELMs.

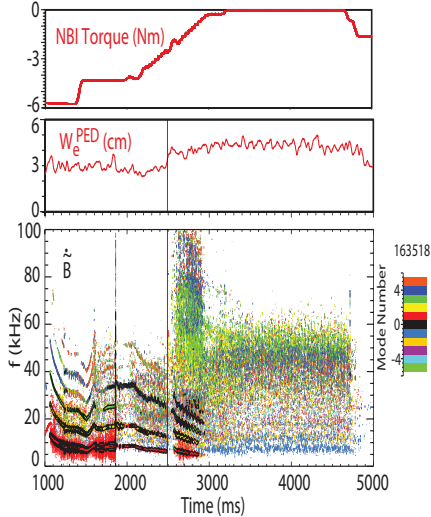


FIG. 3. Pedestal width bifurcation during torque ramp down in QH-mode.

Further advances have been made in the performance of low torque QH-mode at higher q_{95} . In particular, in a balanced double-null shape, the plasma is found to bifurcate to a new state at low torque, characterized by a significantly higher and wider pedestal (Fig. 3). In these conditions, the wide pedestal QH-mode has been extended to higher $\beta_N \approx 2.3$ and $H_{98(y,2)} \approx 1.6$. Measurements find that the $E \times B$ shear in the steep gradient region is reduced at low torque, which enables broadband turbulence to reduce the edge pressure gradients and, consequently, produce the wider pedestal [15, 12]. Future work will investigate compatibility in single null ITER-like shapes and reduced q_{95} .

B Disruption mitigation

If left unmitigated, full current disruptions would pose a serious threat to the integrity of the vessel components and first wall of ITER. A hierarchical approach is anticipated for preventing disruptions, by designing operating scenarios that minimize the risk of plasma termination, utilizing control schemes to avoid exceeding relevant stability limits, deploying techniques for safe ramp down such as locked mode spin up, and, where necessary, employing a disruption mitigation system (DMS) as a last line of defense. The DMS on ITER must simultaneously prevent damage from localized thermal losses during the thermal quench, excessive forces during the current quench, as well as effectively dissipate any runaway electron (RE) beams that may arise from the disruption.

DIII-D is uniquely equipped with the primary ITER DMS technology, shattered pellet injection (SPI), demonstrating thermal and current quench times that scale to values required for ITER. Relative to massive gas injection (MGI), SPI has shown improved assimilation of the injected impurity species. The first successful demonstration of RE plateau dissipation using SPI has been achieved, although changes in

Perhaps the most attractive solution to the ELM problem is to develop scenarios that are naturally ELM-stable with the required level of performance. QH-mode is one such candidate scenario, and has previously been reported at ITER levels of performance without ELMs [10, 11]. In QH-mode, the transport associated with ELMs is replaced with an edge harmonic oscillation (EHO) that limits the pedestal to just below the peeling-ballooning stability limit. The EHO has previously been postulated to be a saturated kink-peeling mode destabilized by rotation shear. New modeling of a low- n EHO with the 3D resistive MHD code M3D-C1 finds a linear Eigenmode structure that shows good agreement with the experimental characteristics from magnetics and internal fluctuation diagnostics (Fig. 2), and confirms the importance of rotation shear in destabilizing the low- n EHO [12]. Nonlinear simulations with JOEAK and NIMROD produce a low- n saturated state with enhanced particle transport consistent with the experimental observations during QH-mode [13, 14].

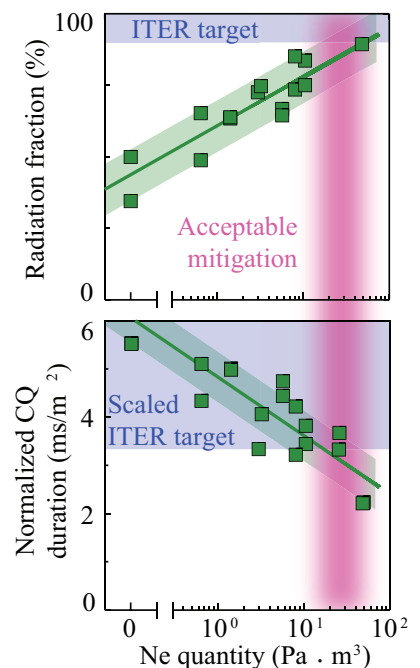


FIG. 4. Radiation fraction and normalized current quench time versus neon quantity using SPI.

the composition of the pellet may be necessary to optimize dissipation properties. The DIII-D results for the mixed species SPI technique show how the disruption properties can be tuned to optimize the trade-off in the radiation fraction and the current quench time (Fig. 4) [16].

Concerns have emerged regarding disruption mitigation in the presence of pre-existing MHD instabilities, since the vast majority of experimental experience has been gained with disruptions triggered by the DMS in otherwise stable plasmas. New experiments on DIII-D show that both MGI and SPI techniques remain effective even in the presence of MHD instabilities, with no significant impact to mitigation of either the thermal or current quench loads [17]. In addition, particle assimilation is not degraded during the thermal quench, the radiation fraction is similar, and the injected impurities remain effective at accelerating the current decay.

DIII-D has deployed a new gamma ray imaging (GRI) diagnostic, a tangentially viewing pinhole camera, to make energy-resolved measurements of the incident gamma ray flux produced [18]. Inversion techniques are used to infer the RE distribution from the measured gamma ray flux. The energy-resolved measurements during controlled dissipation studies in quiescent runaway experiments show different RE growth and dissipation rates at different energies (Fig. 5), revealing that previously observed anomalous dissipation occurs at low energies [19], while runaway growth rates at higher energy are more in line with theoretical predictions. The cause for the anomalous loss at low energy is still under investigation, but one hypothesis is that it is due to magnetic fluctuation-driven radial transport.

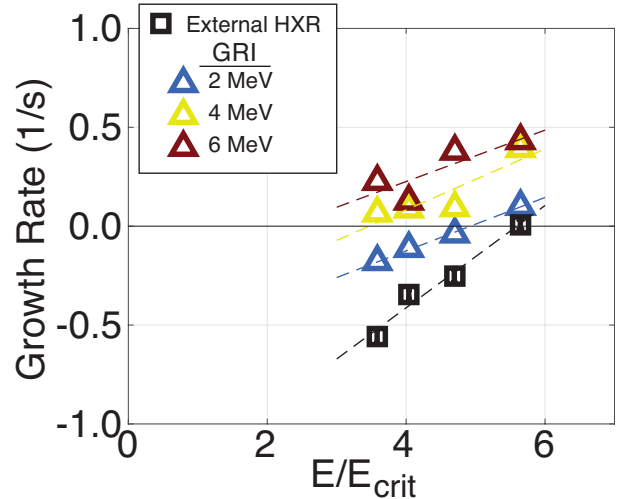


FIG. 5. Energy-resolved growth rate of runaway electrons from GRI as a function of electric field.

3. Preparing for Burning Plasmas

A Achieving $Q = 10$ Performance

DIII-D is developing critical operational experience and scientific understanding to help ITER achieve its primary performance mission. To minimize the distance of extrapolation to ITER, DIII-D continues to extend scenarios toward more relevant conditions. In particular, recent work has focused on both increased heating through the electron transport channel and investigation of low torque stability and confinement.

A degradation in confinement is observed when ECH is added to ITER baseline (IBS) plasmas, associated with increases in both low and higher wavenumber density fluctuations as measured by the beam emission spectroscopy (BES) and Doppler back scattering (DBS) diagnostics. New time-dependent transport simulations using the TGLF transport model successfully reproduce the observed changes in confinement resulting from an increase in intermediate- and high- k TEM- and ETG-scale turbulence, consistent with the fluctuation diagnostics [20, 21]. When TGLF is used to predict the particle transport for ITER, the TEM-scale turbulence results in an inward particle pinch, which in turn leads to a peaked density profile. Simulations with TGLF find the fusion gain is below the $Q = 10$ target when assuming a flat density profile, but this can be recovered by including the predicted peaking of the density. The fusion gain can be increased further by exploiting higher pedestal density, which gives higher pedestal pressure and potentially even access to Super H-mode [22].

The ITER baseline scenario on DIII-D is typically challenged by low- n tearing modes, and at low torque there is a strong tendency for $m/n = 2/1$ tearing modes to slow and lock, often resulting in disruption. The differential rotation between the $q = 2$ and the $q = 3/2$ surface provides a partial separation of stable versus unstable time slices in a database of IBS discharges.

In addition, at low torque and low rotation, the pedestal is typically found to be higher than in the standard co-NBI IBS, resulting in a modification to the bootstrap current and change in the overall current density profile shape at fixed total current. As a result, lower torque plasmas tend to be characterized by a current profile that is more “hollow” in the vicinity of the $q = 2$ surface. Unstable discharges tend to have a larger current gradient inside and outside of the $q = 2$ surface, while stable discharges tend to have a flatter current profile around $q = 2$ [21].

An extension of active MHD spectroscopy (AMS) to IBS conditions has revealed the approach toward an ideal stability limit at low rotation. The plasma magnetic response increases a factor of two to three and the phase shows a sudden change at low rotation. In these IBS plasmas, kinetic effects appear to be significant, with β_N only approximately half of the calculated no-wall limit. Modeling with the fully kinetic MARS-K model with collisionality and resistivity, and the underlying equilibrium kept fixed, partially reproduces the amplitude response as the rotation is lowered, but do not yet capture the response at the lowest rotation levels (Fig. 6). Refinements to the collisionality model in MARS-Q may improve the agreement at very low rotation [21].

Adequate error field correction (EFC) is necessary to minimize unwanted field penetration leading to rotating or locked tearing modes. Recent measurements have indicated that locked mode thresholds for $n = 2$ are similar to $n = 1$ thresholds, with applied field amplitudes comparable to the intrinsic $n = 2$ error field on DIII-D able to trigger a locked $n = 2$ mode. These $n = 2$ modes are typically accompanied by an $n = 1$ mode, and recent studies show the importance of $n > 1$ EFC to avoiding locked modes.

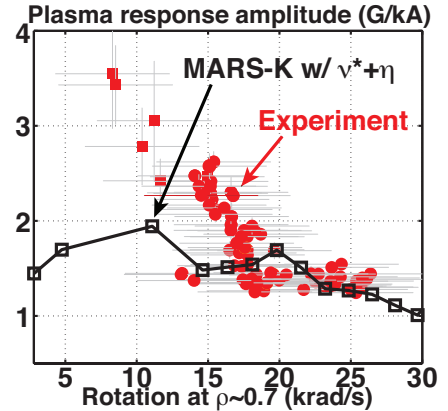


FIG. 6. Plasma magnetic response amplitude versus rotation and comparison with MARS-K.

B Improving transport understanding for projection to burning plasmas

Projecting the results from DIII-D to future burning plasma devices requires a solid physics basis. While there have been many important advances in the understanding of energy transport, it is now being realized that multi-scale turbulence and transport must also be considered, and more attention is also being given to understanding momentum and particle transport.

A key uncertainty for projecting scenarios to future devices is the rotation, which can impact both confinement and stability. Because future large scale devices such as ITER are expected to rotate relatively more slowly from beam-injected torque, the intrinsic drive of rotation may play an important role. Dimensionless scaling experiments have revealed a more favorable ρ^* scaling of the intrinsic torque than expected from theoretical arguments (Fig. 7), and joint experiments with JET and ASDEX-Upgrade have confirmed this scaling [23, 24]. In addition, DIII-D experiments have shown a relatively weak scaling of intrinsic torque with ν^* [25]. These DIII-D results have been combined to yield a projection for the intrinsic torque in ITER that is comparable to the amount injected by neutral beams, although still expected to result in a rotation level that is relatively low for MHD stability.

A flow reversal has been observed in the core of DIII-D L-mode plasmas when ECH is raised above a threshold power, which is correlated with the onset of ITG turbulence. New simulations with the GTS gyrokinetic code accurately reproduce the observed toroidal rotation in the core resulting from a fluctuation-induced “residual stress” (Fig. 8) [24]. Although these measurements and simulations are for L-mode, the gyro-Bohm normalized flux of residual stress in the core of an ITER H-mode may exceed that from the beam driven torque, and hence validation of the

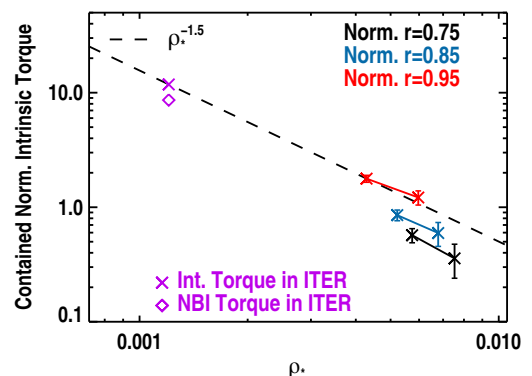


FIG. 7. ρ^* scaling of intrinsic torque projected to ITER.

core residual stress is important for predicting the shear in the rotation profile, which, as noted earlier, can affect stability.

Experiments in hybrid plasmas have demonstrated that ECH power can help prevent the accumulation of argon injected by perturbative gas puff (i.e. impurity “flushing”). Predictions of the argon profile evolution are made using STRAHL to calculate the Ar source and TGLF for the impurity transport coefficients. TGLF underpredicts the turbulent radial transport, resulting in higher argon accumulation and a more peaked argon density profile compared to the experiment. In separate experiments where the temperature is held fixed while the torque is varied, the electron particle transport is affected by the $E \times B$ shearing rate when the shearing rate is below the linear growth rate [26]. The normalized density scale length $R\nabla n/n$ is well-correlated with the frequency of the dominant unstable mode, similar to previous observations on ASDEX-Upgrade [27], with the peaking maximized when the turbulence switches from ITG to TEM (Fig. 9). Nonetheless, analysis suggest that core density peaking can be explained by increased core fueling from neutral beams, rather than due to changes in collisionality, raising doubt about the potential to enhance fusion power in ITER due to the strong density peaking expected from scaling databases [28].

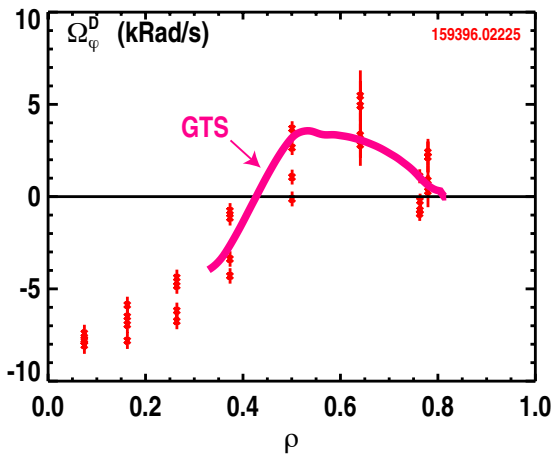


FIG. 8. Comparison of measured main ion rotation with prediction from GTS gyrokinetic simulation of intrinsic drive.

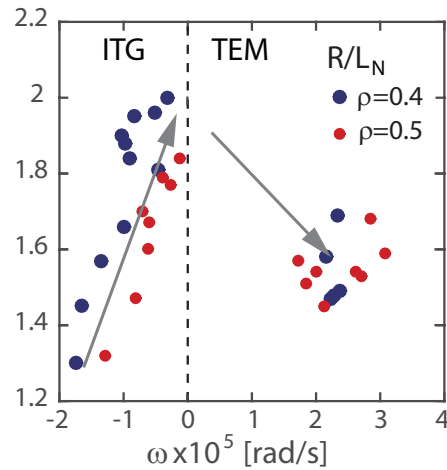


FIG. 9. Degree of density peaking as a function of dominant unstable mode frequency.

New studies on L-H transition physics finds that the L-H power threshold is minimized as a function of density for both hydrogen and deuterium plasmas when two counter-propagating broadband turbulence modes are present [29]. These modes are located just inside the separatrix, giving rise to an increase in poloidal flow shear that enhances turbulence suppression and facilitates the transition. At densities below the minimum in the power, only the ion direction propagating mode is presented, while above the minimum, only the electron mode persists. In hydrogen plasmas, the appearance of the dual mode occurs at higher density than in deuterium plasmas, which would help explain the mass-dependence in the power threshold. At the L-H transition, the poloidal flow acceleration is found to be quantitatively consistent with expectations from the turbulent Reynolds-stress [30].

4. Developing the Necessary Boundary Solutions for Fusion

A Advances in physics of detachment

Diagnostic capability unique to DIII-D has been used to show that drifts are responsible for in-out asymmetries and shifts in the radial profiles in the divertor leg, a result that is directly illustrated through the reversal of the toroidal field and associated $E \times B$ drifts. The measured temperature and density asymmetries have been reproduced with the UEDGE code in H-mode discharges and point to the interplay between radial and poloidal $E \times B$ drifts (Fig. 10) [31].

A persistent “radiation shortfall” has been observed between modeling and experiments in both L- and H-mode deuterium plasmas. Some hypotheses have emerged to explain the discrepancy, which include missing carbon radiation from chemical sputtering, and molecular deuterium and atomic physics contributions not being adequately treated. New modeling with SOLPS of recent helium L-mode plasmas indicates that the shortfall is largely eliminated provided the density in the divertor is well-matched to the experiment. This is consistent with previous modeling of molecular deuterium being the issue in standard deuterium plasmas, and future experiments using the divertor SPRED spectrometer will further quantify this. However, in order to produce a well-matched divertor, $\approx 50\%$ higher upstream density than is measured was required in the modeling. This shows that parallel transport also plays an important role in radiation shortfall when upstream data are used to constrain the models, and suggests that the models may be missing contributions to the total SOL pressure balance (e.g. underestimating ion contributions) [31, 32].

Measurements in near double-null plasmas find that the peak heat flux at the outer divertor target of the primary divertor scales as $q_{\perp} \propto (P_{\text{SOL}} I_p)^{0.92}$, where P_{SOL} is the power through the SOL, consistent with the ITPA scaling originating mostly from single null plasmas (Fig. 11). At very high power and $\beta_N > 3.7$, the addition of D_2 gas as part of a puff-and-pump radiative divertor is found to result in a more significant increase in density than typically observed, in part due to a reduction of the ELM frequency. Such stronger effective core fueling sets an upper limit to the D_2 gas flow in DIII-D to maintain density control in a high β_N discharge with puff-and-pump radiative divertor, and may represent an additional challenge for the technique in very high performance plasmas. In these high β_N discharges, the energy confinement actually increases with D_2 gas flow, with β_N rising to nearly 4 at fixed power [33].

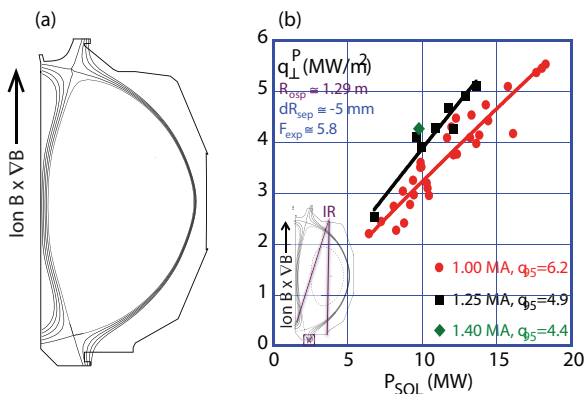


FIG. 11. Peak heat flux in lower divertor as a function of power.

The more advanced divertor geometry referred to as the X-divertor shows detachment at lower upstream density than standard divertor operation. At present, it is believed that the negative gradient in the poloidal field at the target (i.e. flaring) together with an increased

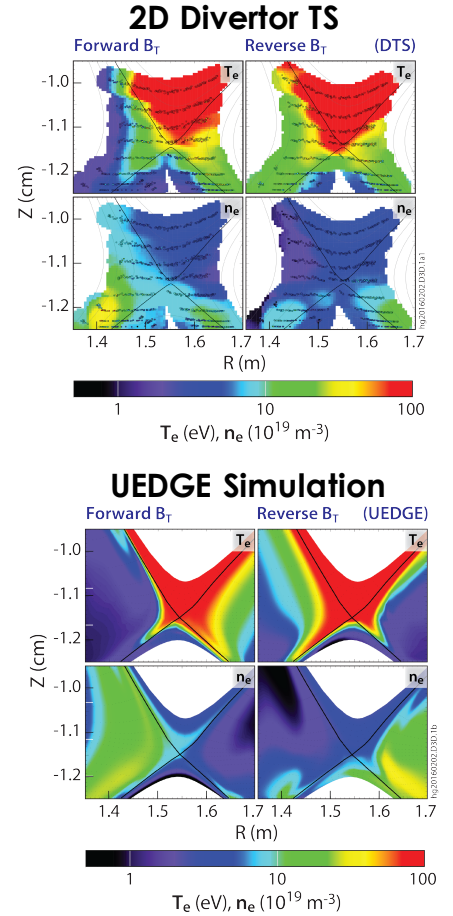


FIG. 10. Comparison of measured 2d density and temperature with modeling with UEDGE in forward and reverse B_T .

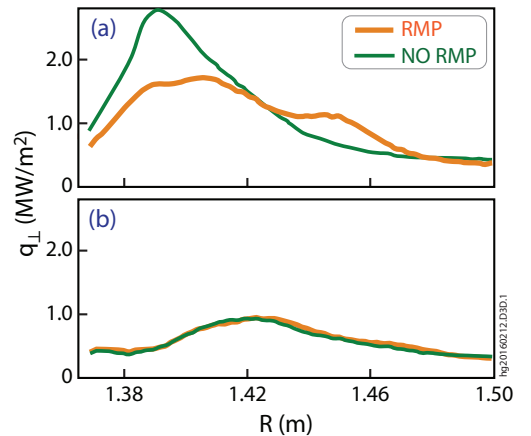


FIG. 12. Heat flux profile with and without RMP at (a) low and (b) high density.

connection length through the high neutral region at the target is responsible for facilitating this detachment at lower density.

A concern has emerged regarding the use of 3D fields (as might be envisioned for ELM control), because RMP fields had been observed to create non-axisymmetric heat flux striations, which can lead to high levels of heat flux on less well armored divertor regions. However, new experiments on DIII-D have shown that these effects can be eliminated by typical dissipative processes at high densities, and the resultant heat flux profile is essentially identical either with or without RMP fields (Fig. 12). Moreover, the additional structure in the electron temperature is also eliminated at high density. In simulations where only the density is varied, the observed reduction in non-axisymmetric divertor flux structures can be qualitatively reproduced. This provides further evidence that the desired suppression of ELMs using RMPs may be compatible with the elimination of non-axisymmetric structures in the divertor [34].

B Interplay between divertor, SOL and pedestal

Comparison of the pedestal profile in the DIII-D closed upper divertor to the more open lower divertor shows that the more closed geometry exhibits an electron pedestal density profile with shallower gradient and lower height. This in turn results in a higher electron temperature pedestal (Fig. 13). Modeling shows that the more closed geometry results in a higher fraction of neutrals ionized in the divertor and a 30% reduction in the pedestal ionization source in otherwise similar divertor plasma conditions without auxiliary gas fueling. These differences remain even as fueling is increased, resulting in a 20% reduction in the pedestal density at detachment in the more closed divertor. While pedestal pressure and confinement tend to degrade under dissipative divertor operation, this appears to be a consequence of operating at higher collisionality, corresponding to a pedestal that is ballooning limited, and should be overcome in future devices operating at high density but low collisionality on the kink-peeling boundary [35].

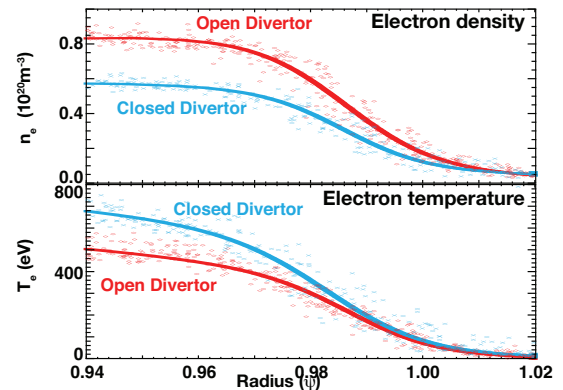


FIG. 13. Comparison of density and temperature profiles between more closed versus open divertor configurations.

C Understanding material erosion and migration

Molybdenum and tungsten samples have been inserted into DIII-D using the Divertor Materials Evaluation System (DiMES) and have shown that the erosion rate is strongly influenced by carbon concentration in the plasma and the magnetic pre-sheath, and can be actively controlled with electrical biasing, as well as by local gas puffing. ERO modeling including a material mixing model indicates that higher carbon concentration leads to more carbon deposition in the mixed material surface layer, which reduces the high- Z material erosion due to surface dilution [36]. $E \times B$ drifts directly impact the low- Z impurity transport and its deposition on high- Z material surfaces. The net erosion profiles on both Mo and tungsten samples are well reproduced by ERO simulations assuming a carbon concentration of 1.8% (Fig. 14). New experiments show that Mo erosion can be reduced more than an order of magnitude when the biasing voltage is close to 40 V. The plasma density and temperature, controlled through localized gas puffing, can also modify the net erosion of high- Z material, as lower temperature and higher density result in a lower sputtering yield but higher carbon deposition in the surface [37].

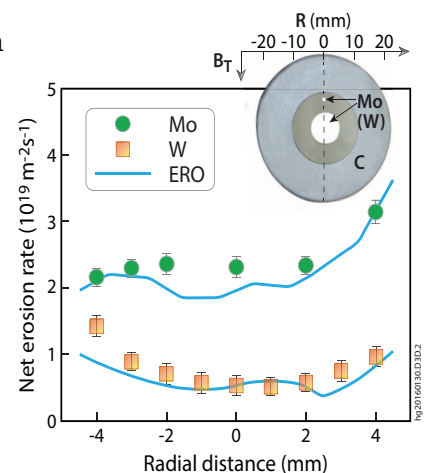


FIG. 14. Experimentally measured radial profiles of net erosion rate for Mo and W and comparison with ERO modeling.

New experiments have recently been performed using complete toroidal rings of W-coated metal inserts at two poloidal locations in the lower outer divertor to quantify high- Z divertor erosion and migration, together with the impact on core scenarios. The W source was strongly impacted by the divertor characteristics, including ELM size, ELM frequency, flux expansion and location of the strike point. In high power, near-steady-state hybrid discharges, utilizing strong on-axis EC power for current drive, W accumulation was not observed, and the performance was essentially identical to cases without the metal rings. This is in contrast to other scenarios such as high- q_{\min} , which tends to use off- rather than on-axis EC power, and consequently did not benefit from ECH “flushing” described in Sec. 3B that inhibits impurity accumulation [38].

5. On the Path to Steady-State Operation

A Development of High Performance Steady-State Scenarios

Significant advances have been made in developing an integrated core-edge solution using the steady-state hybrid regime. Previous work established it as a potentially attractive scenario, with simultaneous high $\beta_N \approx 3.7$ and high confinement $H_{98(y,2)} \approx 1.6$ achieved with zero loop voltage in a double null shape [39]. More recently, complete ELM suppression was achieved in lower $\beta_N \approx 3$ plasmas with an ITER similar shape using odd parity $n = 3$ fields with modest impact on performance ($\approx 5\%$ reduction in $H_{98(y,2)}$ and $\approx 10\%$ in pedestal pressure). Unlike at lower q_{95} for the IBS, ELM suppression is achieved over a wide range in q_{95} ($6 \lesssim q_{95} \lesssim 7.5$) in the steady-state hybrid (Fig. 15). Simulation suggests this benefits from an increased plasma response due to the higher beta, relative to the ITER baseline. New experiments have also demonstrated that high performance can be maintained with an argon puff-and-pump radiative divertor at $\beta_N \approx 3$, which enables radiated power above 50%, peak heat flux in the upper outer divertor reduced by a factor of two, and with less than a 10% increase in Z_{eff} and less than a 5% reduction in confinement [40].

Part of the attraction of the steady-state hybrid is that it can take advantage of on-axis current drive, with an anomalous process redistributing the current to give a broad q -profile associated with excellent confinement and stability. A new technique has been developed to quantify this process by comparing the poloidal flux driven by the coils and the poloidal flux converted to kinetic energy [41]. When there is no $m/n = 3/2$ tearing mode, the two measures of poloidal flux are in agreement and there is no anomaly in the current profile. However, in the presence of the mode, a difference emerges, sufficient to drive up to 10% of the current. Separate experiments and simulation utilizing applied 3D fields indicate this can arise due to a 3-wave interaction causing a helical distortion of the plasma core [42].

Separately, a high bootstrap fraction, high β_P ($\lesssim 4$) scenario has been developed in collaboration with EAST [43], with a large radius internal transport barrier (ITB) operating fully non-inductively at $q_{95} \approx 12$ and maintaining good confinement and stability even at reduced torque. New fluctuation measurements corroborate transport is predominantly neoclassical, with no long wavelength turbulence detected. Turbulence is suppressed due to the large Shafranov shift (rather than $E \times B$ shear) in these high β_P plasmas. Both experiments and ideal stability calculations suggest that wall stabilization is important in this scenario, i.e. the ITB is observed to expand to larger radius at higher β_N , which in general improves the wall-stabilization and enables higher β_N . The scenario characteristics have also been maintained when the plasma current is increased inductively, suggesting that a stable, fully non-inductive scenario at lower

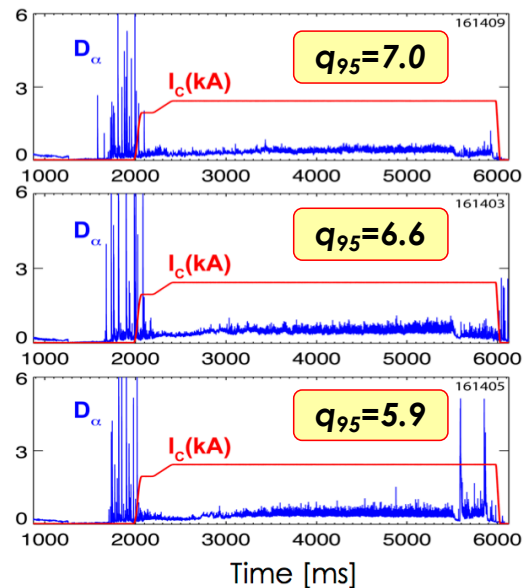


FIG. 15. Demonstration of RMP ELM suppression in steady-state hybrid plasmas over a range in q_{95} .

q_{95} should be feasible. Projections to ITER suggest the high bootstrap fraction scenario will be fully non-inductive at lower $q_{95} \approx 6$, $\beta_P \approx 2.1$ and $\beta_N \approx 2.9$, and can potentially reach $Q = 5$ if confinement of $H_{98(y,2)} \approx 1.6$ is achieved. Analysis suggests this might be feasible with a stronger reverse shear current profile to compensate the lower β_P and Shafranov shift [44].

In separate high- q_{\min} experiments at lower q_{95} , high confinement ($H_{98(y,2)} \approx 1.5$) and improved stability up to $\beta_N \approx 4$ is achieved when $q_{\min} > 2$ and with negative central shear (NCS). These are limited in β by the ideal wall stability limit as predicted by MHD theory, provided other instabilities including resistive wall modes and tearing modes are avoided. Stability analysis indicates higher limits are possible at lower ℓ_i [45], validating the planned path for further improvement through off-axis current drive. To further this goal in a reactor, DIII-D is also exploring very high harmonic fast waves (“helicon”) at 500 MHz in plasmas with high electron beta [46]. An initial low power test of a comb-line type antenna with 12 modules revealed good coupling, and research is ready to proceed to a 1 MW system to test non-linear dynamics [47].

B Control of thermal and fast ion transport

New experiments demonstrate that a broad current profile with NCS is effective in mitigating confinement degradation associated with increasing the electron to ion temperature ratio T_e/T_i , with the T_i profile maintained as ECH is added, unlike observations in standard positive shear plasmas. The difference can be explained in terms of the turbulence, with both simulations and measurements showing that increases in T_e/T_i have less impact on the fluctuation levels in NCS plasmas (Fig. 16) [48].

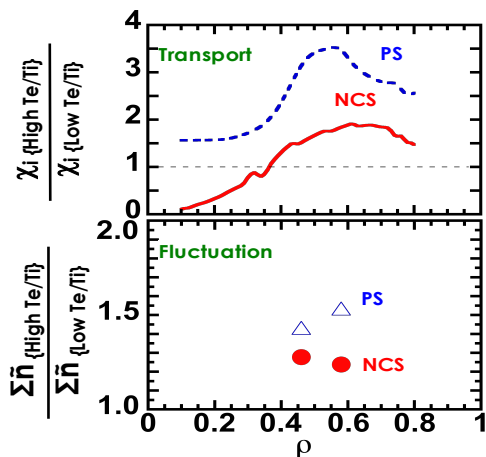


FIG. 16. Relative changes in (a) ion heat diffusivity and (b) density fluctuations between high and low T_e/T_i for positive and negative central shear.

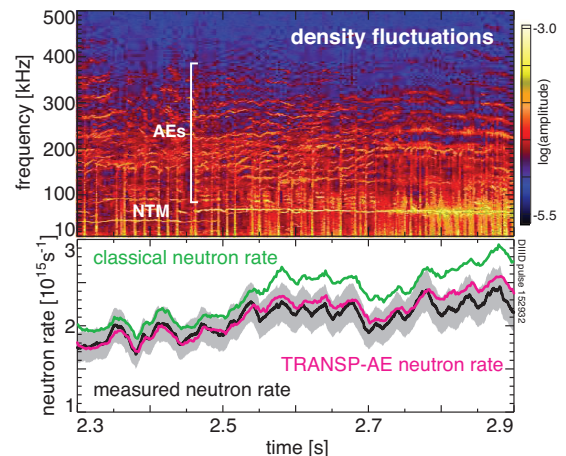


FIG. 17. Comparison of measured neutron rate with classical calculation and from new phase space resolved “kick-model”.

In high q_{\min} plasmas, increased fast ion transport has been observed, which is now understood to be the result of multiple unstable Alfvén Eigenmodes that can lead to “stiff” fast ion transport above a critical gradient. Intermittent losses are observed above the threshold and the fast ion density profile remains relatively unchanged even as the source power is increased [49, 50]. In such cases, the neutron rate is over-predicted with TRANSP using classical slowing down and pitch angle scattering. A new phase-space resolved “kick-model” has been developed and implemented in TRANSP to take into account the resonant effects of multiple modes and the fast ions. With this improved model, the neutron rate is accurately reproduced (Fig. 17) [51]. The poor fast ion confinement is calculated to be a consequence of an undesirable alignment between the fast ion pressure gradient and q_{\min} , and both simulations and experiments show that moving q_{\min} to larger radius, where the fast ion pressure gradient is less steep, can effectively mitigate the anomalous fast ion transport, an effect that appears to be in play in the high β_P

scenario. This further validates the path for broadening the current to develop high performance scenarios.

In the steady-state hybrid scenario, the addition of central ECCD suppresses fast ion instabilities, somewhat similar to previous work that found a dramatic impact on Alfvén Eigenmode activity when EC power is deposited in the vicinity of the location of q_{\min} . In cases with reverse shear, careful studies have revealed the origin of the impact of EC power on Alfvén Eigenmode stability. It is found that increased electron heating raises the GAM frequency, which governs the window for RSAE instability. This model successfully distinguishes between plasmas with strong TAE+RSAE activity versus those with a spectrum of weaker TAE fluctuations [52].

6. Summary and Future Plans

This paper has described key advances in understanding, and demonstration of important principles necessary for the path to realizing fusion energy. RMP-ELM suppression is found to be correlated with exciting an edge current driven mode, while core tearing mode drives are mediated through a global kink response. A more complete understanding of QH-mode has been developed, with modeling confirming the EHO as a saturated kink-peeling instability destabilized by $E \times B$ shear. Shattered pellet injection, the technique selected for disruption mitigation on ITER, has demonstrated runaway electron dissipation for the first time and shown improved impurity assimilation compared with massive gas injection.

Stability remains a challenge for the IBS on DIII-D at low torque, where $m/n = 2/1$ tearing modes are generally observed to be triggered. Active MHD spectroscopy has been successful in detecting the approach to instability in the low torque IBS. New studies show a more favorable ρ^* scaling for the intrinsic rotation drive than might be expected from theory, giving rise to a torque that may be comparable to that from neutral beams on ITER. ECH power is found useful for preventing accumulation of both moderate- and high- Z impurities, and density peaking in low collisionality plasmas appears driven by stronger beam particle fueling.

New diagnostic capability has shown the critical role of drifts in driving in-out asymmetries in the divertor legs. The previously observed “radiation shortfall” is largely eliminated in helium plasmas, provided that the divertor density is reproduced. However, this requires anomalously high upstream pressure, indicating that both parallel transport and atomic/molecular physics are critical in resolving the radiation “shortfall” issue in the modeling. 3D striations observed in the divertor with applied RMPs are eliminated at higher density approaching detachment.

ELM-suppression has been achieved in fully non-inductive steady-state hybrid plasmas, with relative insensitivity to q_{95} , and only small impact on confinement and performance. The high β_p scenario maintains high confinement levels even at low levels of torque, understood by the fact that the turbulence is suppressed by high β Shafranov stabilization. Anomalous fast ion transport is understood to result from stiff transport above a critical gradient, which can be overcome by moving the location of q_{\min} to larger radius.

Future plans include a modification to the upper divertor on DIII-D for testing several principles of closure, as well as exploiting a new optimized geometry dubbed “small angle slot” (SAS) that aims to achieve detachment at reduced upstream density and lower temperatures across the entire target, important for an advanced divertor solution. A second SPI system using a three-barrel ITER prototype design [53] is currently being installed on DIII-D, which will allow investigation of pellet synchronization and multiple pellet injections from toroidally distinct locations to provide valuable information in preparation for operation on ITER. New power supplies have been provided through a collaboration with ASIPP that will enable increased flexibility of 3D coils for improved transient control. During a planned long torus opening beginning in the latter half of 2017, a second neutral beam line will be modified to deliver additional off-axis current drive, which together with increased ECCD power will be exploited to push toward a fully non-inductive high q_{\min} scenario with $\beta_N \approx 4.5$ to help resolve the path to steady-state. There is also consideration for further validation of the helicon approach for driving off-axis current with a high power antenna installation.

This work was supported by the US Department of Energy under DE-FC02-04ER54698.

DIII-D data shown in this paper can be obtained in digital format by following the links at https://fusion.gat.com/global/D3D_DMP.

References

- [1] ZOHRM, H., Plasma Phys. Control. Fusion **38** (1996) 105.
- [2] EVANS, T. E. et al., Phys. Rev. Lett. **92** (2004) 235003.
- [3] LANG, P. T. et al., Nucl. Fusion **43** (2003) 1110.
- [4] BAYLOR, L. et al., Nucl. Fusion **49** (2009) 085013.
- [5] BURRELL, K. H. et al., Phys. Plasmas **8** (2001) 2153.
- [6] PAZ-SOLDAN, C. et al., this conference, EX/1-2 .
- [7] NAZIKIAN, R. et al., this conference, EX/PD .
- [8] SHAFER, M. et al., this conference, EX/P3-18 .
- [9] BORTOLON, A. et al., this conference, EX/10-1 .
- [10] GAROFALO, A. M. et al., Phys. Plasmas **22** (2015) 056116.
- [11] SOLOMON, W. M. et al., Nucl. Fusion **55** (2015) 073031.
- [12] CHEN, X. et al., this conference, EX/3-2 .
- [13] LIU, F. et al., this conference, TH/P1-9 .
- [14] KING, J., this conference, TH/P1-8 .
- [15] BURRELL, K. H. et al., Phys. Plasmas **23** (2016) 056103.
- [16] COMMAUX, N. et al., this conference, EX/9-2 .
- [17] SHIRAKI, D. et al., this conference, EX/P3-20 .
- [18] PACE, D. C. et al., Rev. Sci. Instrum. **87** (2016) 043507.
- [19] PAZ-SOLDAN, C. et al., Phys. Plasmas **21** (2014) 022514.
- [20] HOLLAND, C. et al., this conference, TH/6-1 .
- [21] TURCO, F. et al., this conference, EX/P3-14 .
- [22] SOLOMON, W. M. et al., Phys. Plasmas **23** (2016) 056105.
- [23] TALA, T. et al., 43rd European Physical Society Conference on Plasma Physics (2016) .
- [24] GRIERSON, B. et al., this conference, EX/11-1 .
- [25] CHRYSTAL, C. et al., to be submitted to Phys. Plasmas (2016) .
- [26] WANG, X. et al., Plasma Phys. Control. Fusion **58** (2016) 045026.
- [27] ANGIONI, C. et al., Nucl. Fusion **52** (2012) 114003.
- [28] MORDIJCK, S. et al., this conference, EX/P3-9 .
- [29] YAN, Z. et al., this conference, EX/5-1 .
- [30] SCHMITZ, L. et al., this conference, EX/P3-11 .
- [31] MCLEAN, A. et al., this conference, EX/2-1 .
- [32] CANIK, J. et al., to be submitted to Phys. Plasmas (2016) .
- [33] PETRIE, T. et al., this conference, EX/P3-27 .
- [34] BRIESEMEISTER, A. et al., this conference, EX/7-3Rb .
- [35] LEONARD, A. et al., this conference, EX/P3-25 .
- [36] DING, R. et al., Nucl. Fusion **56** (2016) 016021.
- [37] DING, R. et al., this conference, MPT/1-2Rb .
- [38] UNTERBERG, E. et al., this conference, EX/PD .
- [39] TURCO, F. et al., Phys. Plasmas **22** (2015) 056113.
- [40] PETTY, C. et al., this conference, EX/4-1 .
- [41] LUCE, T. C. et al., Nuclear Fusion **54** (2014) 93005.
- [42] PIOVESAN, P. et al., this conference, EX/1-1 .
- [43] GAROFALO, A. M. et al., Nucl. Fusion **55** (2015) 123025.
- [44] QIAN, J. P. et al., this conference, EX/4-2 .
- [45] HANSON, J. et al., this conference, EX/P3-15 .
- [46] PRATER, R. et al., Nucl. Fusion **54** (2014) 083024.
- [47] PINSKER, R. et al., this conference, EX/P3-22 .
- [48] YOSHIDA, M. et al., this conference, EX/8-1 .
- [49] COLLINS, C. S. et al., Phys. Rev. Lett. **116** (2016) 95001.
- [50] COLLINS, C. S. et al., this conference, EX/6-2 .
- [51] KRAMER, G. et al., this conference, TH/P4-5 .
- [52] VAN ZEELAND, M. et al., this conference, EX/P3-24 .
- [53] BAYLOR, L. R., Fusion Sci. And Technol. **68** (2015) 211.

Appendix: The DIII-D team

G. Abela¹, T. Abrams¹, J.W. Ahn², E. Allen¹, S.L. Allen³, G. Ambrosino⁴, J.P. Anderson¹, N. Asakura⁵, M.E. Austin⁶, D. Ayala¹, S.-G. Baek⁷, C.P. Balance⁸, M.J. Baldwin⁹, K. Barada¹⁰, L. Bardoczi¹⁰, J.E. Barton¹¹, J.L. Barton¹², E.M. Bass¹³, D.J. Battaglia¹³, L.R. Baylor², E.A. Belli¹, R. Bengtson⁶, L.J. Bergsten¹⁴, N. Bertelli¹³, J. Bialek¹⁵, M. Bobrek², J.A. Boedo⁹, R.L. Boivin¹, N.G. Bolte¹⁶, P. Bonoli⁷, J.E. Boom¹⁷, A. Bortolon¹³, C. Bowman¹⁸, M.D. Boyer¹³, R.V. Bravenec¹⁹, B.D. Bray¹, D.P. Brennan²⁰, S. Brezinsek²¹, A.R. Briesemeister², M.W. Brookman⁶, J.N. Brooks²², D.L. Brower¹⁰, B.R. Brown¹, E.W. Bryerton²³, D.A. Buchenauer¹², R.V. Budny¹³, K.H. Burrell¹, R.J. Buttery¹, I. Bykov⁹, I.L. Caldas²⁴, J.D. Callen²⁵, R.W. Callis¹, G.L. Campbell¹, G.P. Canal¹, J. Candy¹, J.M. Canik², L. Cao²⁶, M. Capella⁹, A. Cappa²⁷, T.N. Carlstrom¹, W. Carpanese²⁸, D. Carralero¹⁷, T.A. Carter¹⁰, W.P. Cary¹, L. Casali¹, M. Cengher¹, V.S. Chan¹, C.S. Chang¹³, I.T. Chapman²⁹, S. Che⁶, J. Chen¹⁰, J. Chen²⁶, M. Chen³⁰, X. Chen¹, Y. Chen³¹, W. Choi¹⁵, B. Choski³², L. Chousal⁹, C.P. Chrobak¹, C. Chrystal¹, R.M. Churchill¹³, M.R. Cianciosa², D. Ciro²⁴, I.G.J. Classen³³, M.D. Clement⁹, C.S. Collins¹, S.K. Combs², N. Commaux², C.M. Cooper¹⁸, W.A. Cooper³⁴, B. Covele¹, E.N. Coviello¹, N.A. Crocker¹⁰, B.J. Crowley¹, L. Cui¹³, I. Cziegler⁹, S. Danani³², B.J. Dannels², E.M. Davis⁷, M. De Angeli³⁵, P. de Marne³⁶, G. De Tommasi⁴, P. de Vries³⁷, J. Decker³⁸, J.S. deGrassie¹, G.Z. Deng²⁶, A. Diallo¹³, P.H. Diamond⁹, A.M. Dimitis³, R. Ding¹⁸, S.Y. Ding²⁶, W.X. Ding¹⁰, J.L. Doane¹, R.P. Doerner⁹, C.W. Domier³⁰, D. Donovan³⁹, C.W. Dormier³⁰, P. Dougherty²³, E.J. Doyle¹⁰, D. Du¹, H. Du⁴⁰, M.C. Dunne¹⁷, N.W. Eidietis¹, J.D. Elder⁴¹, D. Eldon²⁰, R.A. Ellis¹³, R.M. Ellis³, W. Elwasif², D.A. Ennis⁸, D.R. Ernst⁷, S. Ethier¹³, T.E. Evans¹, C. Favreau⁸, W. Feng²⁶, M.E. Fenstermacher³, N.M. Ferraro¹³, J.R. Ferron¹, D. Finkenthal⁴², R.K. Fisher¹, B. Fishler¹, R. Fitzpatrick⁶, S.M. Flanagan¹, R.J. Fonck²⁵, C.R. Foust², E. Fredrickson¹³, H. Frerichs²⁵, D. Fu³⁰, G.-Y. Fu¹³, J. Galdon³⁶, F. Garcia¹, F.J. Garcia-Lopez³⁶, M. Garcia-Munoz³⁶, A.M. Garofalo¹, K.W. Gentle⁶, S.P. Gerhardt¹³, E.P. Gilson¹³, F. Glass¹, P. Gohil¹, X.Z. Gong²⁶, N.N. Gorelenkova¹³, M. Gorelenkova¹³, Y. Gorelov¹, R.S. Granetz⁷, T.K. Gray², D.L. Green²², C.M. Greenfield¹, M. Greenwald⁷, B.A. Grierson¹³, R.J. Groebner¹, M. Groth⁴³, H.L. Grunloh¹, H.Y. Guo¹, W.F. Guo²⁶, J. Guterl¹, W. Guttenfelder¹³, T. Guzman¹, S.H. Hahn⁴⁴, F.D. Halpern¹, M. Hansink¹, J.M. Hanson¹⁵, S.R. Haskey¹³, L. Hausamann¹³, R.J. Hawryluk¹³, C.C. Hegna²⁵, W.W. Heidbrink¹⁶, R.R. Hernandez⁹, D.N. Hill¹, D.L. Hillis², E. Hinson²⁵, S.P. Hirshman², M. Hoelzl¹⁷, C.T. Holcomb³, C. Holland⁹, E.M. Hollmann⁹, I. Holod¹⁶, K. Holtrop¹, A.R. Horton², J. Howard⁴⁵, N. Howard⁷, N.T. Howard⁴⁶, S.C. Hsu⁷¹, F. Hu³⁰, X. Hu³⁰, Y.J. Hu²⁶, J. Huang²⁶, Y. Huang²⁶, A.E. Hubbard⁷, J.W. Hughes⁷, G.T.A. Huijsmans¹³, D.A. Humphreys¹, P. Huynh¹, A.W. Hyatt¹, K. Ida⁴⁷, R. Ikeda⁵, Y. In⁴⁸, S. Inagaki⁴⁹, K. Itoh⁴⁷, S.-I. Itoh⁴⁹, O. Izacard⁹, V.A. Izzo⁹, G.L. Jackson¹, E.F. Jaeger⁵⁰, S.C. Jardin¹³, A.E. Jarvinen³, F. Jenko¹⁰, T.C. Jernigan², M.C. Jimenez-Ramos³⁶, C.A. Johnson⁸, R.D. Johnson¹, I. Joseph³, D.H. Kaplan¹, Y. Kawano⁵, S. Kaye¹³, R. Ke⁷³, A.G. Kellman¹, D.H. Kellman¹, K. Kim², J.D. King⁵¹, A. Kirschner²¹, W.-H. Ko⁴⁴, T. Kobayashi⁴⁷, E.R. Koch¹, E. Kolemen²⁰, M. Kostuk¹, M. Kotschenreuther⁶, G.J. Kramer¹³, S.I. Krasheninnikov⁹, J.A. Kulchar¹, B. LaBombard⁷, R.J. LaHaye¹, J. Lai³⁰, T. Lambot⁵², M.J. Lanctot⁵¹, R. Lantsov¹⁰, L.L. Lao¹, A. Lasa², C.J. Lasnier³, C.H. Lau², P. Lauber¹⁷, M. Lauret¹¹, S.A. Lazerson¹³, B.P. LeBlanc¹³, R.L. Lee¹, X. Lee¹, M. Lehnen³⁷, A.W. Leonard¹, E. Li²⁶, G.Q. Li²⁶, M. Li²⁶, L. Liang²⁶, Z. Lin¹⁶, J.B. Lister³⁴, C. Liu¹, F. Liu¹³, H. Liu²⁶, J.B. Liu²⁶, Y.Q. Liu²⁹, A. Loarte³⁷, S.D. Loch⁸, N.C. Logan¹³, J. Lohr¹, J.D. Lore², Z.X. Lu⁹, T.C. Luce¹, N.C. Luhmann³⁰, C.J. Luna⁵³, A.E.L. Lunniss⁵⁴, R. Lunsford¹³, G.N. Luo²⁶, B.C. Lyons¹⁸, B. Lyv²⁶, J.E. Maggs¹⁰, S. Mahajan⁶, R. Maingi¹³, M.A. Makowski³, M. Mamidanna³⁰, D.K. Mansfield¹³, S. Mao²⁵, M. Margo¹, A. Marinoni⁷, E.S. Marmor⁷, L. Marrelli⁵⁵, P. Martin⁵⁵, M. Mattei⁴, P. Mauzey¹, J. McClenaghan¹⁸, A. McCubbin⁵⁶, G.R. McKee²⁵, A.G. McLean³, S.J. Meitner¹⁸, J.E. Menard¹³, O. Meneghini¹, W.H. Meyer³, D. Miller¹, C.P. Moeller¹, G.J. Morales¹⁰, S. Mordijck⁵⁷, A.L. Moser¹, R.A. Moyer⁹, D. Mueller¹³, T.L. Munsat³¹, M. Murakami², C. Murphy¹, C.M. Muscatello¹, C.E. Myers¹³, L. Myrabo⁵⁸, A. Nagy¹³, M. Nakata⁴⁷, A.B. Navarro¹⁰, G.A. Navratil¹⁵, R. Nazikian¹³, G. Neu¹⁷, X. Nguyen¹⁰, M. Nocente⁵⁹, S. Noraky¹, J.-M. Noterdaeme¹⁷, R.E. Nygren¹², M. O'Mullane⁶⁰, Y. Oda⁵, S. Ohdachi⁴⁷, M. Okabayashi¹³, K.E.J. Olofsson¹⁸, M. Ono⁶¹, D.M. Orlov³, T.H. Osborne¹, L. Owen², N.A. Pablant¹³, R. Paccagnella⁵⁵, D.C. Pace¹, C.K. Pan²⁶, J.-K. Park¹³, J.M. Park², C. Parker¹, S.E. Parker³¹, K.L. Parkin⁵², P.B. Parks¹, G. Pautasso¹⁷, C.J. Pawley¹, C. Paz-Soldan¹, W.A. Peebles¹⁰, B.G. Penafior¹, J. Penna⁷, E.A.D. Persico¹⁶, T.W. Petrie¹, C.C. Petty¹, Y. Peysson³⁸, A.-V. Pham³⁰, T. Phan³⁰, A.Yu. Pigarov⁹, D. Pince¹, R.I. Pinsker¹, P. Piovesan⁵⁵, L. Piron⁵⁵, R.A. Pitts³⁷, M. Podesta¹³, F. Poli¹³, D. Ponce¹, M. Porkolab⁷, G.D. Porter³, R. Prater¹, J.P. Qian²⁶, C. Rapson¹⁷, S. Ratynskaia⁶², J.M. Rauch¹, P. Raum⁶³, G. Raupp¹⁷, C. Rea⁷, A.H. Reiman¹³, H. Reimerdes³⁴, M.L. Reinke², Q.L. Ren²⁶, X. Ren³⁰, T.L. Rhodes¹⁰, P. Ricci³⁴, J.E. Rice⁷, L. Riford¹¹, M.A. Riso⁶⁴, G. Riva³⁵, P. Rodriguez-Fernandez⁷, M. Rodriguez-Ramos³⁶, T.D. Rognlien³, A. Romosan⁶⁵, A.L. Roquemore¹³, J.C. Rost⁷, W.L. Rowan⁶, D.L. Rudakov⁹, D. Ryan²⁹, D.D. Ryutov³, K. Sakamoto⁵, A. Salmi⁶⁶, B. Sammulu¹, C.M. Samuel³, L. Sanchis-Sanchez³⁶, C.F. Sang⁴⁰, D.P. Schissel¹, L. Schmitz¹⁰, O. Schmitz²⁵, E. Schuster¹¹, J.T. Scoville¹, S.K. Seal², M.W. Shafer², S.E. Sharapov²⁹, S.K. Sharma³², H. Sheng⁶⁷, M. Shephard⁶⁸, L. Shi¹³, W. Shi¹¹, S. Shiraiwa⁷, D. Shiraki², A. Shoshani⁶⁵, H. Si²⁶, D. Smith²⁵, S.P. Smith¹, A. Snicker¹⁷, J.A. Snipes³⁷, P.B. Snyder¹, W.M. Solomon¹, A.C. Sontag², V.A. Soukhanovskii³, A.G. Spear³⁰, D. Spong², W.M. Stacey⁷⁰, G.M. Staebler¹, L. Stagner¹⁶, P.C. Stangeby⁴¹, E. Startsev¹³, R. Stempok¹, J. Stillerman⁷, D.P. Stotler¹³, E.J. Strait¹, X. Sun²⁶, C. Sung¹⁰, W. Suttrop¹⁷, Y. Suzuki⁴⁷, R. Sweeney¹⁵, S. Taimourzadeh¹⁶, K. Takahashi⁵, T. Tala⁶⁶, H. Tan²⁶, W.M. Tang¹³, R.L. Tanna³², D. Taussig¹, G. Taylor¹³, N.Z. Taylor¹⁸, P. Taylor¹, T.S. Taylor¹, J.L. Terry⁷, D.M. Thomas¹, K.E. Thome¹⁸, A. Thorman⁴⁵, A.J. Thorton²⁹, A. Tinguely⁷, B.J. Tobias¹³, P. Tolias⁶², J.F. Tooker¹, H. Torrealba¹, A.C. Torrezan¹, W. Treutterer¹⁷, D.D. Truong²⁵, D. Tskhakaya⁶⁹, C.K. Tsui⁹, F. Turco¹⁵, A.D. Turnbull¹, G.R. Tynan⁹, M.V. Umansky³, E.A. Unterberg², P. Valanju⁶, E. Valeo¹³, M.A. VanZeeland¹, B.S. Victor³, R. Vieira⁷, F.A. Volpe¹⁵, M.S. Vorenkamp¹³, M.R. Wade¹, J. Walk⁷, M.I. Walker¹, G. Wallace⁷, R.E. Waltz¹, W.R. Wampler¹², B.N. Wan²⁶, W. Wan³¹, G. Wang¹⁰, H. Wang²⁶, H.Q. Wang¹⁸, L. Wang²⁶, Q. Wang⁷⁴, W.X. Wang¹³, X. Wang⁵⁷, Z. Wang⁴⁶, Z.R. Wang¹³, C. Wamberg¹⁰, J.G. Watkins¹², W.P. Wehner¹¹, A.S. Welande¹, A.E. White⁷, R.B. White¹³, R.S. Wilcox², T. Wilks⁷, H.R. Wilson⁵⁴, A. Wingen², A. Winter³⁷, S. Wolfe⁷, C.P.C. Wong¹, G.M. Wright⁷, J. Wright⁷, K.J. Wu⁶⁵, W. Wu¹, S. Wukitch⁷, B.J. Xiao²⁶, W.W. Xiao⁷⁵, Y. Xie²⁶, G.S. Xu²⁶, X. Xu³, Z. Yan²⁵, S. Yang⁴⁰, M. Yoshida⁵, L. Yu⁶, Q. Yuan²⁶, M. Zach², P. Zanca⁵⁵, Q. Zang²⁶, S. Zemedkun³¹, L. Zeng¹⁰, B. Zhang²⁶, F. Zhang⁶⁸, X. Zhao⁹, Y. Zhao⁷², Y.B. Zhu¹⁶

Affiliations

- ¹General Atomics
- ²Oak Ridge National Laboratory
- ³Lawrence Livermore National Laboratory
- ⁴CREATE/Seconda Universit di Napoli
- ⁵National Institutes for Quantum and Radiological Science and Technology
- ⁶University of Texas Austin
- ⁷Massachusetts Institute of Technology
- ⁸Auburn University
- ⁹University of California San Diego
- ¹⁰University of California Los Angeles
- ¹¹Lehigh University
- ¹²Sandia National Laboratory
- ¹³Princeton Plasma Physics Laboratory
- ¹⁴Dartmouth College
- ¹⁵Columbia University
- ¹⁶University of California Irvine
- ¹⁷Max-Planck-Institut fr Plasmaphysik
- ¹⁸Oak Ridge Associated Universities
- ¹⁹Fourth State Research
- ²⁰Princeton University
- ²¹Forschungszentrum Jlich GmbH
- ²²Purdue University
- ²³Virginia Diodes, Inc.
- ²⁴Universidade de So Paulo
- ²⁵University of Wisconsin-Madison
- ²⁶Institute of Plasma Physics, Chinese Academy of Sciences
- ²⁷Laboratorio Nacional de Fusion-CIEMAT
- ²⁸Politecnico di Milano
- ²⁹CCFE Fusion Association
- ³⁰University of California Davis
- ³¹University of Colorado
- ³²Institute for Plasma Research, India
- ³³Dutch Institute for Fundamental Fusion Energy Research
- ³⁴CRPP Lausanne
- ³⁵Instituto di Fisica del Plasma
- ³⁶University of Seville
- ³⁷ITER Organization
- ³⁸CEA
- ³⁹University of Tennessee
- ⁴⁰Dalian University of Technology
- ⁴¹University of Toronto
- ⁴²Palomar Scientific Instruments
- ⁴³Aalto University
- ⁴⁴NFRI
- ⁴⁵Australia National University
- ⁴⁶Oak Ridge Institute for Science and Education (ORISE)
- ⁴⁷National Institute for Fusion Science
- ⁴⁸FAR-TECH
- ⁴⁹Kyushu University
- ⁵⁰XCEL Engineering, Inc.
- ⁵¹US Department of Energy
- ⁵²Carnegie Mellon University
- ⁵³Arizona State University
- ⁵⁴University of York
- ⁵⁵Consorzio RFX
- ⁵⁶Hope College
- ⁵⁷College of William and Mary
- ⁵⁸Lightcraft Technologies, Inc.
- ⁵⁹Universita degli Studi di Milano-Bicocca
- ⁶⁰University of Strathclyde
- ⁶¹The Graduate University for Advanced Studies (SOKENDAI)
- ⁶²KTH Royal Institute of Technology
- ⁶³Virginia Tech
- ⁶⁴State University of New York-Buffalo
- ⁶⁵Lawrence Berkeley National Laboratory
- ⁶⁶Association EURATOM-Tekes
- ⁶⁷Peking University
- ⁶⁸Rensselaer Polytechnic Institute
- ⁶⁹University of Innsbruck
- ⁷⁰Georgia Tech
- ⁷¹Los Alamos National Laboratory
- ⁷²Suzhou University
- ⁷³Tsinghua University
- ⁷⁴Zhejiang University
- ⁷⁵Southwestern Institute of Physics